

# Exploring Frustration Effects of Strongly Interacting Bosons via the Hall Response

Catalin-Mihai Halati<sup>1</sup> and Thierry Giamarchi<sup>1</sup>

<sup>1</sup>*Department of Quantum Matter Physics, University of Geneva, Quai Ernest-Ansermet 24, 1211 Geneva, Switzerland*  
(Dated: May 30, 2024)

We investigate the Hall response of hardcore bosonic atoms on a triangular ladder in a magnetic field. We show that the behavior of the Hall polarization, both in its saturation value and in the short-time dynamics, correlates with the features of the underlying phase diagram. In particular, it exhibits a strong negative response at the Meissner to vortex phase transitions, while at large magnetic fluxes, after changing sign, it shows a strong positive response due to non-trivial vortex commensurability effects stemming from the interplay of interactions and geometric frustration. Thus, one can employ the Hall response as a sensitive probe of the many-body chiral quantum phases present in the system.

Strongly correlated quantum systems exhibit an intricate interplay between various energy scales and degrees of freedom. This makes the systems susceptible to perturbations and driving, opening the opportunity for probing and controlling their dynamics to investigate novel quantum behaviors [1]. In particular, in low dimensional frustrated quantum systems, the presence of different interactions which cannot be simultaneously satisfied can give rise to quantum phases with exotic ordering [2–5]. Due to advancements in the field of ultracold atoms in optical lattices [6–11], such frustrated triangular geometries have been the focus of recent experimental studies [12–18].

One of the most important transport measurements over time has been the Hall effect. It has proven to have implications way beyond the naive derivation relating its value to the number of carriers [19]. In the case of non-interacting systems, the Hall response has been related to topological invariants of quantum systems and the curvature of Fermi surface [20, 21]. At large magnetic fields, phenomena such as the Integer Quantum Hall effect [22, 23] have found their place in metrology. In contrast, many open questions remain regarding the deep impact of interactions on the Hall effect. When the magnetic field is very large, the existence of a gap between Landau levels leads to the appearance of the Fractional Quantum Hall effect [24, 25] and to fractional excitations [26], a direct consequence of the strong correlations existing in the system. When the field is small, and a gap does not protect the excitations in the bulk of the material, the situation is even more mysterious. Theoretical studies have partly addressed this question for strongly correlated systems of bosons or fermions making use of special geometries [27–29].

Investigations for ladder systems, made of coupled one-dimensional structures, have allowed to access the Hall effect for interacting systems [30–32]. In particular, in the past few years it was shown that for interacting ladders the Hall imbalance and Hall voltage could be determined reliably from numerical calculations [32, 33], leading to a *universal* behavior related to the number of carriers for large values of the interactions, or interchain tunnelling.

The ultracold atoms implementation of artificial gauge fields and synthetic dimensions [34, 35], and their experimental realizations [36–44], led to a successful test of the predictions for a ladder of interacting fermionic atoms [44]. This paves the way to quantitative investigations of the Hall effect of correlated systems. Furthermore, analytical studies for a square ladder [45] confirmed the universal behavior for Galilean invariant systems, and established a generic relation between the Hall resistance and charge stiffness, hinting that the Hall response should be a particularly sensitive probe for phase transitions in correlated systems.

However, the previous studies have been done for quantum systems in which the kinetic energy does not lead by itself to frustration effects, which can lead to very different properties under a magnetic field. Triangular ladders, either spin ones [46–50], or itinerant bosonic, or fermionic ones under flux [51–63], have been shown to exhibit phase transitions that have no direct equivalent in the square ladders [59]. In addition, in two dimensions the Hall effect has proven to be affected by the frustration on triangular lattices [64–66]. Thus, it is interesting to explore the properties of the Hall effect in the novel situation of frustrated flux ladders.

In this work, we undertake such a study for a triangular ladder of strongly interacting bosonic atoms under the action of a magnetic field. In this regard, we harness the Hall response in order to investigate the non-trivial effects stemming from frustration. Employing extensive numerical simulations based on matrix product states, we show that the Hall response is an extremely sensitive probe of the features present throughout the phase diagram. Furthermore, the non-equilibrium dynamical behavior can be used to fingerprint the many-body chiral phases and the intriguing frustration effects, stemming from the interplay of hardcore interactions, magnetic flux and triangular geometry.

We study bosonic atoms with hardcore interactions confined to a triangular ladder in an artificial gauge field, as sketched in Fig. 1(a). The Bose-Hubbard Hamiltonian

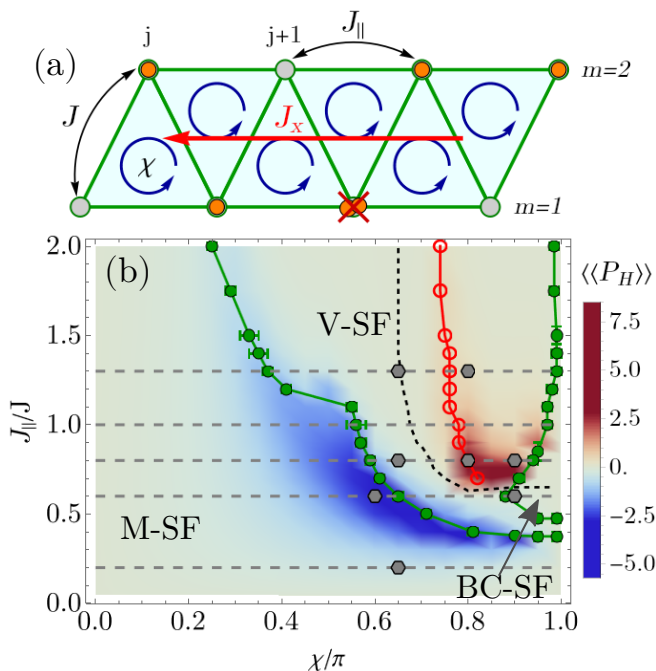


FIG. 1: (a) Sketch of the triangular ladder setup, where the legs are numbered by  $m = 1, 2$  and the sites on each leg by  $j$ . The bosonic atoms can tunnel along the legs with amplitude  $J_{\parallel}$  and along the rungs with amplitude  $J$ . We consider a hardcore on-site interaction between the atoms, and each triangular plaquette to be pierced by a flux  $\chi$ . We pass a current  $\mathbf{J}_x$  through the ladder by applying a linear potential  $V_x$ . (b) The value of the time-averaged Hall polarization  $\langle\langle P_H \rangle\rangle$  as a function of  $J_{\parallel}/J$  and  $\chi$ . The density of the hardcore atoms is  $\rho = 0.25$ , the system size  $L = 90$  and linear potential  $\mu/J = 0.001$ . Green circles and curves denote the phase boundaries. Red disks mark the maximum of the commensurate frequency peak in the rung currents [67]. With the dashed black curve we mark the positions where  $\langle\langle P_H \rangle\rangle \approx 0$ . Gray hexagons and lines correspond to the parameters presented in Fig. 2 and Fig. 3.

of the system is given by [59]

$$H = -J \sum_{j=1}^L \left( b_{j,1}^{\dagger} b_{j,2} + b_{j+1,1}^{\dagger} b_{j,2} + \text{H.c.} \right) - J_{\parallel} \sum_{j=1}^{L-1} \left( e^{-i\chi} b_{j,1}^{\dagger} b_{j+1,1} + e^{i\chi} b_{j,2}^{\dagger} b_{j+1,2} + \text{H.c.} \right) \quad (1)$$

The bosonic annihilation and creation operators  $b_{j,m}$  and  $b_{j,m}^{\dagger}$  act at position  $j$  and leg  $m = 1, 2$ . The atomic density is given by  $\rho = N/(2L)$ , where  $N = \sum n_{j,m}$  is the total number of atoms and the ladder has  $L$  sites on each leg. The tunneling has amplitude  $J_{\parallel}$  along the two legs of the ladder and  $J$  along the rungs. The complex factor in the hopping stems from the artificial magnetic field, with flux  $\chi$  [34, 35]. The atoms experience hardcore on-site interactions, such that at most one particle can be found in each site. We assume  $\hbar = 1$  in the following. For

this system of interacting bosonic atoms on the triangular ladder we have previously determined that the ground state phase is extremely rich [59], containing for example Meissner (M-SF) and vortex (V-SF) chiral superfluid phases, and phases particular to the triangular geometry, like the biased chiral superfluid (BC-SF). Furthermore, going beyond the parameters considered in Ref. [59] we highlight the existence also of vortex lattice superfluids (VL-SF) in the triangular flux ladder with vortex densities of  $\rho_v = 0.6$  and  $\rho_v = 0.8$  (see Supplemental [67]).

We take the system out of equilibrium by quenching a linear potential in the  $x$ -direction,  $V_x = \mu \sum_{j=1}^L \sum_{m=1}^2 \left[ j + \frac{1}{2}(m-1) \right] n_{j,m}$ . This protocol determines a Hall response in the system [32, 33] as in the following. We start at time  $t = 0$  in the ground state of the Hamiltonian  $H$ , Eq. (1). After the quench with the potential  $V_x$ , for  $t > 0$ , a current develops in the  $x$ -direction,  $\mathbf{J}_x$ , and, in the presence of the magnetic flux, a density imbalance between the two legs of the ladder,  $P_y = \sum_j (n_{j,1} - n_{j,2})$ . For the triangular ladder geometry the current  $\mathbf{J}_x$  is defined as [67]

$$\mathbf{J}_x = -i \sum_j \left[ \frac{J}{2} \left( b_{j,1}^{\dagger} b_{j,2} + b_{j,2}^{\dagger} b_{j+1,1} - \text{H.c.} \right) + J_{\parallel} \left( e^{-i\chi} b_{j,1}^{\dagger} b_{j+1,1} + e^{i\chi} b_{j,2}^{\dagger} b_{j+1,2} - \text{H.c.} \right) \right]. \quad (2)$$

We note that a negative sign of  $\mathbf{J}_x$  corresponds to a current flowing downstream with respect to the linear potential i.e. towards smaller values of the site index  $j$ . The Hall response of the system is given by the ratio of the two observables, namely the Hall polarization defined as [32, 33]

$$P_H(t) = \frac{\langle P_y \rangle(t)}{\langle \mathbf{J}_x \rangle(t)/J}. \quad (3)$$

For the BC-SF phase which shows a finite value of the imbalance in equilibrium, in the numerator we consider the difference with respect to the ground state,  $\langle P_y \rangle(t) - \langle P_y \rangle(0)$ . In order to compute  $P_H(t)$  we simulate the time-evolution of the system starting from the ground state in the absence of the potential, using an approach based on time-dependent matrix product state methods (tMPS) (see Supplemental for further details [67]). After the quench of the linear potential, generically, the magnitude of the density imbalance and the current  $\mathbf{J}_x$  grow in time until the finite size effects start to influence the dynamics [67]. However, interestingly, the Hall polarization, after a short time dynamics, exhibits a transient saturation (see Supplemental [67] and Fig. 2). This allows us, as for previous studies on square ladders [32, 33], to study this steady value as a function of the parameters of the model, see Fig. 1(b). In the following, we denote by the Hall polarization  $\langle\langle P_H \rangle\rangle$  the late time average of  $P_H(t)$ , where we performed the average over a time interval of at least  $10/J$ .

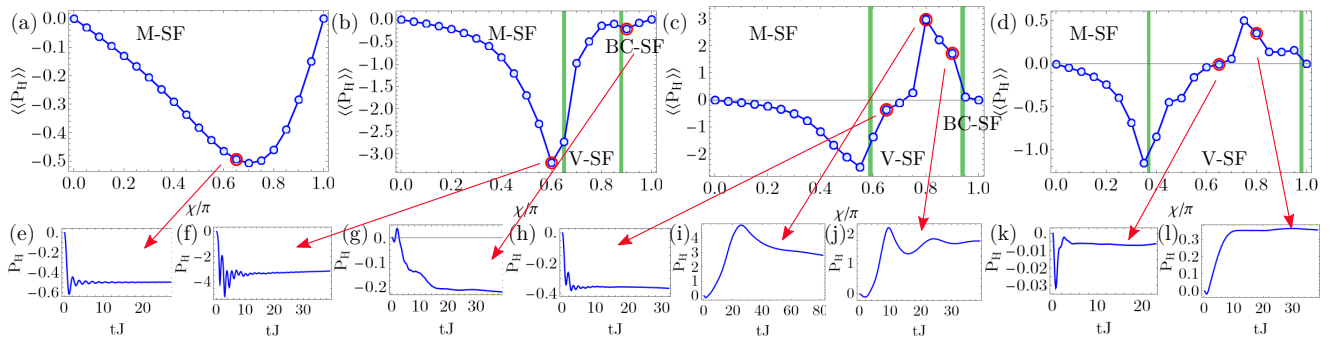


FIG. 2: (a)-(d) Time-averaged Hall polarization  $\langle\langle P_H \rangle\rangle$  as a function of  $\chi$  for the following parameters  $J_{\parallel}/J \in \{0.2, 0.6, 0.8, 1.3\}$ . The green vertical lines mark the phase boundaries between M-SF, V-SF and BC-SF phases. (e)-(l) Time dependence of  $P_H$  for: (e) M-SF,  $J_{\parallel}/J = 0.2$ ,  $\chi = 0.65$ ; (f) M-SF,  $J_{\parallel}/J = 0.6$ ,  $\chi = 0.6$ ; (g) BC-SF,  $J_{\parallel}/J = 0.6$ ,  $\chi = 0.9$ ; (h) V-SF,  $J_{\parallel}/J = 0.8$ ,  $\chi = 0.65$ ; (i) V-SF,  $J_{\parallel}/J = 0.8$ ,  $\chi = 0.8$ ; (j) V-SF,  $J_{\parallel}/J = 0.8$ ,  $\chi = 0.9$ ; (k) V-SF,  $J_{\parallel}/J = 1.3$ ,  $\chi = 0.65$ ; (l) V-SF,  $J_{\parallel}/J = 1.3$ ,  $\chi = 0.8$ . The system size used is  $L = 90$  rungs, filling  $\rho = 0.25$  and the strength of the linear potential  $\mu/J = 0.001$ .

We begin our analysis by investigating the dependence of  $\langle\langle P_H \rangle\rangle$  as a function of the magnetic flux  $\chi$  and the hopping along the legs  $J_{\parallel}$ , as shown in Fig. 1(b). We superimpose the values computed for the Hall polarization with the phase boundaries determined in the ground state of the model, plotted with green points in Fig. 1(b). The interplay between the frustration induced by the triangular geometry, the magnetic flux and the hardcore interactions gives rise to multiple chiral phases in the ground state [59]. For the results presented in Fig. 1 and Fig. 2 we consider a filling of  $\rho = 0.25$  and obtain the following phases (see [67] for the details in determination of the phase diagram): the Meissner superfluid (M-SF), characterized by strong chiral currents on the legs and the absence of currents on the rungs; vortex superfluid (V-SF), for which the currents form a vortex pattern incommensurate with the underlying lattice; and the biased-chiral superfluid (BC-SF), state specific to the triangular ladder, which breaks the  $\mathbb{Z}_2$  symmetry of the ladder and is characterized by a density imbalance.

From the values of  $\langle\langle P_H \rangle\rangle$  plotted in Fig. 1(b) we can identify several features of interest, which strongly correlate with the highlights of the ground state phase diagram. We first observe that starting in the M-SF an increasingly stronger response is obtained as one moves towards the V-SF phase, with a large negative peak in  $\langle\langle P_H \rangle\rangle$  agreeing very well with the equilibrium phase transition line between the Meissner and vortex states. In the regime of large flux  $\chi$ , where the frustration effects dominate, the Hall polarization can change sign [black dashed line in Fig. 1(b)] both in the V-SF and BC-SF phases. Intriguingly,  $\langle\langle P_H \rangle\rangle$  shows also a large positive peak for  $J_{\parallel}/J \gtrsim 0.7$ , which matches the phase boundary between the vortex and biased phases and the presence of a commensurate dependence of the currents in the vortex phase [red symbols in Fig. 1(b)]. In order to understand better these features of the Hall response we investigate the behavior of  $\langle\langle P_H \rangle\rangle$  as a function of  $\chi$

for several values of  $J_{\parallel}/J$ , marked by dashed gray lines in Fig. 1(b) and shown Fig. 2(a)-(d), together with the time-dependence  $P_H(t)$  for several parameter sets, gray hexagons in Fig. 1(b) and depicted in Fig. 2(e)-(l).

In contrast to the square ladder, for the triangular geometry, at small values of  $J_{\parallel}/J$  the Meissner superfluid phase can be found for any value of  $\chi$  [59]. In the M-SF the time dependence of  $P_H$  exhibits a rapid increase, followed an oscillatory regime which dampens on an time interval of around  $10/J$  towards a steady value, see Fig. 2(e). The dynamics is very similar to the one obtained for the Meissner phase on the square ladder [32, 33]. If we monitor  $\langle\langle P_H \rangle\rangle$  in the regime of small  $J_{\parallel}/J$  we obtain a curve which vanishes at  $\chi = 0, \pi$  and has a maximum  $\chi \approx 0.5\pi$ . However, if we increase  $J_{\parallel}/J$ , e.g. in Fig. 2(a) for  $J_{\parallel}/J = 0.2$ , the height of the maximum increases and moves towards larger values of the flux. This behavior is determined by the proximity of the phase transition to the vortex phase, as we can see in Fig. 2(b) for  $J_{\parallel}/J = 0.6$ , where as a function of the flux we have a transition at  $\chi \approx 0.65\pi$ . We can observe that approaching the phase transition in the M-SF the Hall polarization exhibits a divergence-like behavior towards very large values. In the time dependence of  $P_H$  for  $\chi = 0.6\pi$  we can see a different profile, Fig. 2(f), especially in the short-time oscillatory dynamics, compared to when we are further away from the transition in the M-SF. This large value of  $\langle\langle P_H \rangle\rangle$  is due a decrease in the value current  $\mathbf{J}_x$  at the transition [67]. Interestingly, this behavior stems from single particle effects at the M-SF to V-SF transition, and survives up to the strongly interacting many-body regimes. This is supported by the dependence on the density shown in Fig. 3(a) for  $J_{\parallel}/J = 1$ , with the divergent behavior being more pronounced for lower densities and present even for the case of a single particle (black curve).

One of the highlights of the ground state of the Hamiltonian, Eq. (1), is the presence of the BC-SF phase at

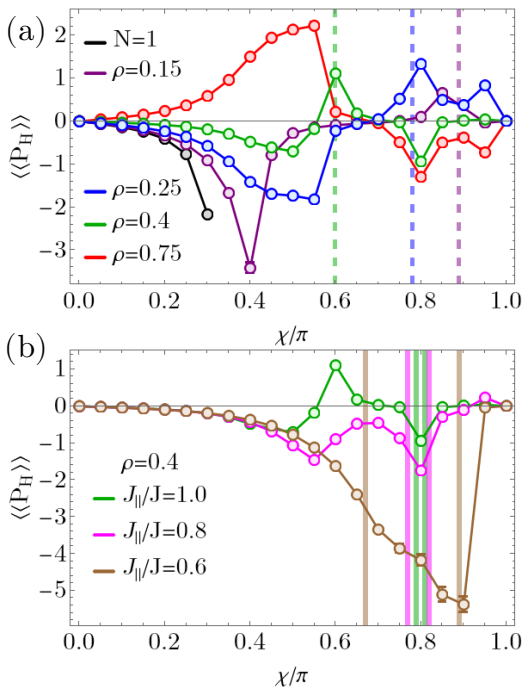


FIG. 3: Time-averaged Hall polarization  $\langle\langle P_H \rangle\rangle$  as a function of  $\chi$  for (a) different values of the filling  $\rho$  at  $J_{\parallel}/J = 1$ , (b) different values of  $J_{\parallel}/J$  at  $\rho = 0.4$ . In (a) the vertical dashed lines mark the maximum of the commensurate peak in the rung currents, with the respective colors. In (b) the vertical lines mark the phase boundaries of the VL-SF with  $\rho_v = 0.8$ .

large values of  $\chi$ , particular to the frustrated triangular geometry. Thus, it is an interesting question to determine how the Hall polarization behaves in this phase. As the BC-SF appears for large values of the flux,  $\chi \gtrsim 0.87\pi$  in Fig. 2(b) and  $\chi \gtrsim 0.93\pi$  in Fig. 2(c), the magnitude of the Hall polarization is lower than in some of the other phases. The dynamics of  $P_H(t)$  in the BC-SF, Fig. 2(g), shows a very distinct behavior, different than in the M-SF. At short times we observe multiple sign changes, followed by a slow evolution towards the steady value, with an intermediate plateau. In this case the main features are determined by the evolution of the imbalance  $P_y$ , with the current showing a mostly linear increase [67]. Furthermore, in this phase we have a two-fold degenerate ground state spanned by states with density imbalances of opposite signs, however, as long as we subtract the initial imbalance, the additional imbalance and the current induced by the linear potential are identical for both states, resulting in the same  $P_H$ .

Another feature present in the BC-SF, and in the V-SF, is the fact that the Hall polarization changes sign within this phases when one increases  $J_{\parallel}$  as seen in Fig. 1(b) (sign change marked by the dashed black line). One possible cause of a sign change in the Hall response is the change of the sign of the charge of the carries, from particles to holes. This can be attributed to the obser-

vation from Fig. 3 that  $\langle\langle P_H \rangle\rangle$  has the same magnitude for  $\rho = 0.25$  and  $\rho = 0.75$  for all values of the flux, but opposite sign. And to the fact that for  $\rho = 0.5$ , in the presence of a particle-hole symmetry, the Hall polarization vanishes. However, we have not identified a similar argument for the change of sign as a function of  $\chi$  or  $J_{\parallel}$ . In the following, we analyze in more details the region of positive values of  $P_H$  in the vortex phase.

In the vortex superfluid we have initially an abrupt drop in the magnitude of  $\langle\langle P_H \rangle\rangle$  after entering from the Meissner phase, as seen in Fig. 2(b)-(d), which further increases towards zero. Close to the transition the dynamics of  $P_H$  looks similar to the M-SF curves, see Fig. 2(h) in contrast with Fig. 2(e)-(f), while for the values of the flux where  $\langle\langle P_H \rangle\rangle$  is close to zero we have a rapid saturation to a small value, Fig. 2(k). After changing sign  $\langle\langle P_H \rangle\rangle$  further increases to positive values, Fig. 2(c)-(d). Furthermore, the positive peak exhibits very different behavior compared to the negative one discussed previously, in the time dependence of  $P_H$  we observe a significant slowing down, see Fig. 2(i)-(j), with the steady plateau appearing at much longer times. For  $J_{\parallel}/J = 0.8$  the stabilization takes place after several slow oscillations [Fig. 2(i)], which are absent for  $J_{\parallel}/J = 1.3$  [Fig. 2(l)].

There are two main candidates for strong positive response, the proximity to the BC-SF phase and the presence of a second commensurate vortex density in the ground state patterns. The closeness seems indeed to be correlated to positive values of  $\langle\langle P_H \rangle\rangle$  for  $0.7 \lesssim J_{\parallel}/J \lesssim 1.1$  [Fig. 1(b)], however the positive peak is also present for larger values of  $J_{\parallel}/J$  where the BC-SF is confined to a very narrow region close to  $\chi = \pi$  [Fig. 2(d) and Fig. 1(b)]. In Ref. [59] we have described in case of hardcore bosons the presence of additional periodicities in the Fourier transform of the ground state rung currents, which lead to commensurate vortex densities of  $\rho_v = \rho$  and  $\rho_v = (1 - \rho)$ , beside the expected incommensurate density  $\rho_v = \chi/\pi$ . Upon closer inspection [67], we find that the Fourier response of the commensurate vortex density of  $\rho_v = (1 - \rho)$  can be comparable, or even dominant, with the respect to the incommensurate one, however, it does not change the nature of the V-SF phase by inducing a gap in one of the two gapless modes. We mark the position where the commensurate vortex density is dominant with red disks in Fig. 1(b). These follow exactly the evolution of the positive peak in  $\langle\langle P_H \rangle\rangle$  in the V-SF as we increase  $J_{\parallel}/J$ . Furthermore, we check this for several values of the density in Fig. 3(a) and we observe a very good agreement. We can obtain further understanding on the commensurate frequency by considering the mapping of hardcore bosons to fermions using the Jordan Wigner transformation,  $b_j = \prod_{i=1}^{j-1} e^{i\pi c_i^\dagger c_i} c_j$ , with  $c_j$  fermionic operators [67]. For hardcore bosons on a chain the transformation results in free fermions. However, if we rewrite our Hamiltonian, Eq. (1), on a chain defined along the rungs we obtain a hopping term

over two sites which results in interaction term in the fermionic language,  $b_j^\dagger b_{j+2} = c_j^\dagger (1 - 2c_{j+1}^\dagger c_{j+1}) c_{j+2}$ . By varying the strength of the four-fermion term we can construct a phase diagram interpolating from free fermions on a triangular flux ladder to the hardcore bosons described by Eq. (1) (see Supplemental [67]). For intermediate values of the interaction, we find a vortex lattice phase with its vortex density determined by the filling,  $\rho_v = 1 - \rho$ . Furthermore, this periodicity of the currents survives the phase transition to the V-SF phase towards the hardcore bosons limit. Thus, the commensurate component of the ground state vortex density stems from the interplay of interactions and triangular geometry, which we observe that it also induces a non-trivial behavior in the Hall polarization.

A strong Hall response in the presence of a commensurate current pattern seems to be characteristic only for the regime where frustration plays an important role,  $\chi \gtrsim 0.5\pi$ . We can emphasize this point by computing the Hall polarization for the genuine vortex lattice phases (VL-SF), characterized by a current pattern commensurate with the triangular ladder, which appear for an atomic filling of  $\rho = 0.4$  [67]. In the regime of  $0.4\pi \lesssim \chi \lesssim 0.5\pi$  at  $J_{\parallel}/J = 1$  we have a VL-SF with  $\rho_v = 0.6$ , however,  $\langle\langle P_H \rangle\rangle$  does not show any abrupt feature, it continues the monotonic decrease started from M-SF up to the V-SF phase [green curve in Fig. 3(a)]. Interestingly, for the filling  $\rho = 0.4$  we observe an additional sign change in  $\langle\langle P_H \rangle\rangle$  followed by a negative peak at  $\chi = 0.8\pi$ . At a closer inspection this is due to the presence of a narrow vortex lattice phase with  $\rho_v = 0.8$  in the ground state. To confirm this, we analyze in Fig. 3(b) the effect of lowering  $J_{\parallel}/J$  which widens the VL-SF. This increases significantly the values at which the Hall polarization stabilizes, for  $J_{\parallel}/J = 0.6$  this manifests itself for a wide window of flux,  $0.7\pi \lesssim \chi \lesssim 0.9\pi$ , not just as a peak around a particular value. This further shows that the interplay of commensurate vortex current structures and frustration can lead to a strong response in the Hall polarization.

In conclusion, we have investigated the Hall response of hardcore bosons in a triangular ladder under the action of a magnetic flux. We show that the saturation value of the Hall polarization following the quench of a linear potential is an extremely sensitive probe of the features of the phase diagram. It exhibits large negative values correlated to the phase transition boundary between M-SF and V-SF. At large values of the flux,  $P_H$  changes sign and exhibits a non-trivial behavior in connection with the commensurability effects present in the V-SF and VL-SF. Furthermore, the non-equilibrium dynamics of the Hall polarization following the quench of the linear potential towards the saturation value depends strongly on the initial quantum phase and can be used as a fingerprint of different chiral phases found in the phase diagram. As the Hall effect has been measured experimentally with ultra-

cold fermionic atoms for square ladders [44] and recently a proposal has been put forward for the implementation of triangular flux ladders [63], we expect that our results on the frustrated triangular ladder are directly relevant to current generation of ultracold atoms experiments.

*Acknowledgments:* We thank J.-S. Bernier, M. Filippone for fruitful discussions. We acknowledge support by the Swiss National Science Foundation under Division II grants 200020-188687 and 200020-219400. This research was supported in part by grant NSF PHY-1748958 to the Kavli Institute for Theoretical Physics (KITP). The authors would like to thank the Institut Henri Poincaré (UAR 839 CNRS-Sorbonne Université) and the LabEx CARMIN (ANR-10-LABX-59-01) for their support.

- 
- [1] D. N. Basov, R. D. Averitt, and D. Hsieh, *Towards properties on demand in quantum materials*, [Nature Materials](#) **16**, 1077 (2017).
  - [2] R. Moessner and A. P. Ramirez, *Geometrical frustration*, [Physics Today](#) **59**, 24 (2006).
  - [3] C. Lacroix, P. Mendels, and F. Mila, *Introduction to frustrated magnetism: materials, experiments, theory* (Springer Berlin, Heidelberg, 2011).
  - [4] L. Balents, *Spin liquids in frustrated magnets*, [Nature](#) **464**, 199 (2010).
  - [5] O. A. Starykh, *Unusual ordered phases of highly frustrated magnets: a review*, [Reports on Progress in Physics](#) **78**, 052502 (2015).
  - [6] M. Lewenstein, A. Sanpera, V. Ahufinger, B. Damski, A. Sen(De), and U. Sen, *Ultracold atomic gases in optical lattices: mimicking condensed matter physics and beyond*, [Advances in Physics](#) **56**, 243 (2007).
  - [7] I. Bloch, J. Dalibard, and W. Zwerger, *Many-body physics with ultracold gases*, [Rev. Mod. Phys.](#) **80**, 885 (2008).
  - [8] J. I. Cirac and P. Zoller, *Goals and opportunities in quantum simulation*, [Nature Physics](#) **8**, 264 (2012).
  - [9] N. Goldman, J. C. Budich, and P. Zoller, *Topological quantum matter with ultracold gases in optical lattices*, [Nature Physics](#) **12**, 639 (2016).
  - [10] W. Hofstetter and T. Qin, *Quantum simulation of strongly correlated condensed matter systems*, [Journal of Physics B: Atomic, Molecular and Optical Physics](#) **51**, 082001 (2018).
  - [11] F. Schäfer, T. Fukuhara, S. Sugawa, Y. Takasu, and Y. Takahashi, *Tools for quantum simulation with ultracold atoms in optical lattices*, [Nature Reviews Physics](#) **2**, 411 (2020).
  - [12] C. Becker, P. Soltan-Panahi, J. Kronjäger, S. Dörscher, K. Bongs, and K. Sengstock, *Ultracold quantum gases in triangular optical lattices*, [New Journal of Physics](#) **12**, 065025 (2010).
  - [13] J. Struck, C. Ölschläger, R. L. Targat, P. Soltan-Panahi, A. Eckardt, M. Lewenstein, P. Windpassinger, and K. Sengstock, *Quantum Simulation of Frustrated Classical Magnetism in Triangular Optical Lattices*, [Science](#) **333**, 996 (2011).
  - [14] J. Yang, L. Liu, J. Mongkolkiattichai, and P. Schauss,

- Site-Resolved Imaging of Ultracold Fermions in a Triangular-Lattice Quantum Gas Microscope*, *PRX Quantum* **2**, 020344 (2021).
- [15] J. Mongkolkiattichai, L. Liu, D. Garwood, J. Yang, and P. Schauss, *Quantum gas microscopy of fermionic triangular-lattice Mott insulators*, *Phys. Rev. A* **108**, L061301 (2023).
- [16] M. Xu, L. H. Kendrick, A. Kale, Y. Gang, G. Ji, R. T. Scalettar, M. Lebrat, and M. Greiner, *Frustration- and doping-induced magnetism in a Fermi-Hubbard simulator*, *Nature* **620**, 971 (2023).
- [17] M. Lebrat, M. Xu, L. H. Kendrick, A. Kale, Y. Gang, P. Seetharaman, I. Morera, E. Khatami, E. Demler, and M. Greiner, *Observation of Nagaoka polarons in a Fermi-Hubbard quantum simulator*, *Nature* **629**, 317 (2024).
- [18] M. L. Prichard, B. M. Spar, I. Morera, E. Demler, Z. Z. Yan, and W. S. Bakr, *Directly imaging spin polarons in a kinetically frustrated Hubbard system*, *Nature* **629**, 323 (2024).
- [19] J. M. Ziman, *Principles of the Theory of Solids*, 2nd ed. (Cambridge University Press, 1972).
- [20] D. Xiao, M.-C. Chang, and Q. Niu, *Berry phase effects on electronic properties*, *Rev. Mod. Phys.* **82**, 1959 (2010).
- [21] D. J. Thouless, M. Kohmoto, M. P. Nightingale, and M. den Nijs, *Quantized Hall Conductance in a Two-Dimensional Periodic Potential*, *Phys. Rev. Lett.* **49**, 405 (1982).
- [22] K. v. Klitzing, G. Dorda, and M. Pepper, *New Method for High-Accuracy Determination of the Fine-Structure Constant Based on Quantized Hall Resistance*, *Phys. Rev. Lett.* **45**, 494 (1980).
- [23] K. von Klitzing, *The quantized Hall effect*, *Rev. Mod. Phys.* **58**, 519 (1986).
- [24] D. C. Tsui, H. L. Stormer, and A. C. Gossard, *Two-Dimensional Magnetotransport in the Extreme Quantum Limit*, *Phys. Rev. Lett.* **48**, 1559 (1982).
- [25] H. L. Stormer, D. C. Tsui, and A. C. Gossard, *The fractional quantum Hall effect*, *Rev. Mod. Phys.* **71**, S298 (1999).
- [26] R. B. Laughlin, *Anomalous Quantum Hall Effect: An Incompressible Quantum Fluid with Fractionally Charged Excitations*, *Phys. Rev. Lett.* **50**, 1395 (1983).
- [27] A. Lopatin, A. Georges, and T. Giamarchi, *Hall effect and interchain magneto-optical properties of coupled Luttinger liquids*, *Phys. Rev. B* **63**, 075109 (2001).
- [28] G. León, C. Berthod, and T. Giamarchi, *Hall effect in strongly correlated low-dimensional systems*, *Phys. Rev. B* **75**, 195123 (2007).
- [29] A. Auerbach, *Hall Number of Strongly Correlated Metals*, *Phys. Rev. Lett.* **121**, 066601 (2018).
- [30] P. Prelovšek, M. Long, T. Markež, and X. Zotos, *Hall Constant of Strongly Correlated Electrons on a Ladder*, *Phys. Rev. Lett.* **83**, 2785 (1999).
- [31] X. Zotos, F. Naef, M. Long, and P. Prelovšek, *Reactive Hall Response*, *Phys. Rev. Lett.* **85**, 377 (2000).
- [32] S. Greschner, M. Filippone, and T. Giamarchi, *Universal Hall Response in Interacting Quantum Systems*, *Phys. Rev. Lett.* **122**, 083402 (2019).
- [33] M. Buser, S. Greschner, U. Schollwöck, and T. Giamarchi, *Probing the Hall Voltage in Synthetic Quantum Systems*, *Phys. Rev. Lett.* **126**, 030501 (2021).
- [34] J. Dalibard, F. Gerbier, G. Juzeliūnas, and P. Öhberg, *Colloquium: Artificial gauge potentials for neutral atoms*, *Rev. Mod. Phys.* **83**, 1523 (2011).
- [35] N. Goldman, G. Juzeliūnas, P. Öhberg, and I. B. Spielman, *Light-induced gauge fields for ultracold atoms*, *Reports on Progress in Physics* **77**, 126401 (2014).
- [36] M. Aidelsburger, M. Atala, S. Nascimbène, S. Trotzky, Y.-A. Chen, and I. Bloch, *Experimental Realization of Strong Effective Magnetic Fields in an Optical Lattice*, *Phys. Rev. Lett.* **107**, 255301 (2011).
- [37] J. Struck, C. Ölschläger, M. Weinberg, P. Hauke, J. Simonet, A. Eckardt, M. Lewenstein, K. Sengstock, and P. Windpassinger, *Tunable Gauge Potential for Neutral and Spinless Particles in Driven Optical Lattices*, *Phys. Rev. Lett.* **108**, 225304 (2012).
- [38] H. Miyake, G. A. Siviloglou, C. J. Kennedy, W. C. Burton, and W. Ketterle, *Realizing the Harper Hamiltonian with Laser-Assisted Tunneling in Optical Lattices*, *Phys. Rev. Lett.* **111**, 185302 (2013).
- [39] M. Atala, M. Aidelsburger, M. Lohse, J. T. Barreiro, B. Paredes, and I. Bloch, *Observation of chiral currents with ultracold atoms in bosonic ladders*, *Nature Physics* **10**, 588 (2014).
- [40] M. Mancini, G. Pagano, G. Cappellini, L. Livi, M. Rider, J. Catani, C. Sias, P. Zoller, M. Inguscio, M. Dalmonte, and L. Fallani, *Observation of chiral edge states with neutral fermions in synthetic Hall ribbons*, *Science* **349**, 1510 (2015).
- [41] M. E. Tai, A. Lukin, M. Rispoli, R. Schittko, T. Menke, D. Borgnia, P. M. Preiss, F. Grusdt, A. M. Kaufman, and M. Greiner, *Microscopy of the interacting Harper-Hofstadter model in the two-body limit*, *Nature* **546**, 519 (2017).
- [42] D. Genkina, L. M. Aycok, H.-I. Lu, M. Lu, A. M. Pineiro, and I. B. Spielman, *Imaging topology of Hofstadter ribbons*, *New Journal of Physics* **21**, 053021 (2019).
- [43] T. Chalopin, T. Satoor, A. Evrard, V. Makhlov, J. Dalibard, R. Lopes, and S. Nascimbene, *Probing chiral edge dynamics and bulk topology of a synthetic Hall system*, *Nature Physics* **16**, 1017 (2020).
- [44] T.-W. Zhou, G. Cappellini, D. Tusi, L. Franchi, J. Paravicini, C. Repellin, S. Greschner, M. Inguscio, T. Giamarchi, M. Filippone, J. Catani, and L. Fallani, *Observation of universal Hall response in strongly interacting Fermions*, *Science* **381**, 427 (2023).
- [45] R. Citro, T. Giamarchi, and E. Orignac, *Hall response in interacting bosonic and fermionic ladders*, arXiv:2404.16973 (2024), arXiv:2404.16973 [cond-mat.mes-hall] .
- [46] T. Hikihara, L. Kecke, T. Momoi, and A. Furusaki, *Vector chiral and multipolar orders in the spin- $\frac{1}{2}$  frustrated ferromagnetic chain in magnetic field*, *Phys. Rev. B* **78**, 144404 (2008).
- [47] J. Sudan, A. Lüscher, and A. M. Läuchli, *Emergent multipolar spin correlations in a fluctuating spiral: The frustrated ferromagnetic spin- $\frac{1}{2}$  Heisenberg chain in a magnetic field*, *Phys. Rev. B* **80**, 140402 (2009).
- [48] S. Furukawa, M. Sato, and S. Onoda, *Chiral Order and Electromagnetic Dynamics in One-Dimensional Multiferroic Cuprates*, *Phys. Rev. Lett.* **105**, 257205 (2010).
- [49] S. Furukawa, M. Sato, S. Onoda, and A. Furusaki, *Ground-state phase diagram of a spin- $\frac{1}{2}$  frustrated ferromagnetic XXZ chain: Haldane dimer phase and gapped/gapless chiral phases*, *Phys. Rev. B* **86**, 094417 (2012).

- (2012).
- [50] H. Ueda and S. Onoda, *Roles of easy-plane and easy-axis XXZ anisotropy and bond alternation in a frustrated ferromagnetic spin- $\frac{1}{2}$  chain*, *Phys. Rev. B* **101**, 224439 (2020).
- [51] T. Mishra, R. V. Pai, S. Mukerjee, and A. Paramekanti, *Quantum phases and phase transitions of frustrated hardcore bosons on a triangular ladder*, *Phys. Rev. B* **87**, 174504 (2013).
- [52] E. Anisimovas, M. Račiūnas, C. Sträter, A. Eckardt, I. B. Spielman, and G. Juzeliūnas, *Semisynthetic zigzag optical lattice for ultracold bosons*, *Phys. Rev. A* **94**, 063632 (2016).
- [53] F. A. An, E. J. Meier, and B. Gadway, *Engineering a Flux-Dependent Mobility Edge in Disordered Zigzag Chains*, *Phys. Rev. X* **8**, 031045 (2018).
- [54] C. Romen and A. M. Läuchli, *Chiral Mott insulators in frustrated Bose-Hubbard models on ladders and two-dimensional lattices: A combined perturbative and density matrix renormalization group study*, *Phys. Rev. B* **98**, 054519 (2018).
- [55] S. Greschner and T. Mishra, *Interacting bosons in generalized zigzag and railroad-trestle models*, *Phys. Rev. B* **100**, 144405 (2019).
- [56] J. Cabedo, J. Claramunt, J. Mompart, V. Ahufinger, and A. Celi, *Effective triangular ladders with staggered flux from spin-orbit coupling in 1D optical lattices*, *The European Physical Journal D* **74**, 123 (2020).
- [57] Y. Li, H. Cai, D.-w. Wang, L. Li, J. Yuan, and W. Li, *Many-Body Chiral Edge Currents and Sliding Phases of Atomic Spin Waves in Momentum-Space Lattice*, *Phys. Rev. Lett.* **124**, 140401 (2020).
- [58] S. Singha Roy, L. Carl, and P. Hauke, *Genuine multipartite entanglement in a one-dimensional Bose-Hubbard model with frustrated hopping*, *Phys. Rev. B* **106**, 195158 (2022).
- [59] C.-M. Halati and T. Giamarchi, *Bose-Hubbard triangular ladder in an artificial gauge field*, *Phys. Rev. Res.* **5**, 013126 (2023).
- [60] L. Barbiero, J. Cabedo, M. Lewenstein, L. Tarruell, and A. Celi, *Frustrated magnets without geometrical frustration in bosonic flux ladders*, *Phys. Rev. Res.* **5**, L042008 (2023).
- [61] B. Beradze and A. Nersisyan, *Spectrum, Lifshitz transitions and orbital current in frustrated fermionic ladders with a uniform flux*, *The European Physical Journal B* **96**, 2 (2023).
- [62] B. Beradze, M. Tsitsishvili, E. Tirrito, M. Dalmonte, T. Chanda, and A. Nersisyan, *Emergence of non-Abelian SU(2) invariance in Abelian frustrated fermionic ladders*, *Phys. Rev. B* **108**, 075146 (2023).
- [63] N. Baldelli, C. R. Cabrera, S. Julià-Farré, M. Aidelsburger, and L. Barbiero, *Frustrated Extended Bose-Hubbard Model and Deconfined Quantum Critical Points with Optical Lattices at the Antimagic Wavelength*, *Phys. Rev. Lett.* **132**, 153401 (2024).
- [64] G. León, C. Berthod, T. Giamarchi, and A. J. Millis, *Hall effect on the triangular lattice*, *Phys. Rev. B* **78**, 085105 (2008).
- [65] J. O. Haerter, M. R. Peterson, and B. S. Shastry, *Strong Correlations Produce the Curie-Weiss Phase of Na<sub>x</sub>CoO<sub>2</sub>*, *Phys. Rev. Lett.* **97**, 226402 (2006).
- [66] J. O. Haerter, M. R. Peterson, and B. S. Shastry, *Finite-temperature properties of the triangular lattice  $t$ - $J$  model and applications to Na<sub>x</sub>CoO<sub>2</sub>*, *Phys. Rev. B* **74**, 245118 (2006).
- [67] See Supplemental Material regarding the details on derivation of the currents in the triangular ladder, the time-dependent matrix product states approach (tMPS), the ground state phase diagram for hardcore bosons, and the time dependence of the Hall polarization. The Supplemental Material includes Refs. [59, 64, 68–77]
- [68] S. R. White and A. E. Feiguin, *Real-Time Evolution Using the Density Matrix Renormalization Group*, *Phys. Rev. Lett.* **93**, 076401 (2004).
- [69] A. J. Daley, C. Kollath, U. Schollwöck, and G. Vidal, *Time-dependent density-matrix renormalization-group using adaptive effective Hilbert spaces*, *Journal of Statistical Mechanics: Theory and Experiment* **2004**, P04005 (2004).
- [70] U. Schollwöck, *The density-matrix renormalization group in the age of matrix product states*, *Annals of Physics* **326**, 96 (2011).
- [71] S. R. White, *Density matrix formulation for quantum renormalization groups*, *Phys. Rev. Lett.* **69**, 2863 (1992).
- [72] M. Fishman, S. R. White, and E. M. Stoudenmire, *The ITensor Software Library for Tensor Network Calculations*, *SciPost Phys. Codebases*, 4 (2022).
- [73] G. Vidal, J. I. Latorre, E. Rico, and A. Kitaev, *Entanglement in Quantum Critical Phenomena*, *Phys. Rev. Lett.* **90**, 227902 (2003).
- [74] P. Calabrese and J. Cardy, *Entanglement entropy and quantum field theory*, *Journal of Statistical Mechanics: Theory and Experiment* **2004**, P06002 (2004).
- [75] C. Holzhey, F. Larsen, and F. Wilczek, *Geometric and renormalized entropy in conformal field theory*, *Nuclear Physics B* **424**, 443 (1994).
- [76] I. Affleck and A. W. W. Ludwig, *Universal noninteger “ground-state degeneracy” in critical quantum systems*, *Phys. Rev. Lett.* **67**, 161 (1991).
- [77] N. Laflorencie, E. S. Sørensen, M.-S. Chang, and I. Affleck, *Boundary Effects in the Critical Scaling of Entanglement Entropy in 1D Systems*, *Phys. Rev. Lett.* **96**, 100603 (2006).

## SUPPLEMENTAL MATERIAL

### Currents in the triangular ladder

In this section, we derive the expressions for the currents  $\mathbf{J}_x$  and  $\mathbf{J}_y$  flowing on the triangular ladder. We note that the expressions are equivalent to the ones obtained on the two-dimensional triangular lattice in Ref. [64]. To determine the currents we add an additional vector potential for the electric field,  $\hat{A} = A_x \hat{x} + A_y \hat{y}$ . This will introduce a Peierls phase in the hopping amplitudes  $J_{l_1 l_2} = J_{l_1 l_2} \exp\left[-i \int_{l_1}^{l_2} \hat{A} d\hat{l}\right]$ , where  $J_{l_1 l_2}$  is the hopping amplitude between two neighboring sites on the triangular ladder  $l_1$  and  $l_2$ . Then the total currents flowing in a certain direction  $\sigma$  are defined as

$$\mathbf{J}_\sigma = \sum_i \left. \frac{\delta H}{\delta A_\sigma(i)} \right|_{\hat{A}=0}. \quad (\text{A.1})$$

Performing the functional derivatives we obtain

$$\begin{aligned} \mathbf{J}_x = -i \sum_j \left[ \frac{J}{2} \left( b_{j,1}^\dagger b_{j,2} + b_{j,2}^\dagger b_{j+1,1} - \text{H.c.} \right) \right. \\ \left. + J_\parallel \left( e^{-i\chi} b_{j,1}^\dagger b_{j+1,1} + e^{i\chi} b_{j,2}^\dagger b_{j+1,2} - \text{H.c.} \right) \right], \end{aligned} \quad (\text{A.2})$$

$$\mathbf{J}_y = -i \sum_j \frac{J\sqrt{3}}{2} \left( b_{j,1}^\dagger b_{j,2} + b_{j+1,1}^\dagger b_{j,2} - \text{H.c.} \right). \quad (\text{A.3})$$

The local currents on the leg  $j_{j,m}^\parallel$  and the rung  $j_j^\perp$  are defined as

$$\begin{aligned} j_{j,m}^\parallel &= -iJ_\parallel \left[ e^{i\chi(-1)^m} b_{j,m}^\dagger b_{j+1,m} - \text{H.c.} \right], \\ j_{2j-1}^\perp &= -iJ(b_{j,1}^\dagger b_{j,2} - \text{H.c.}), \\ j_{2j}^\perp &= -iJ(b_{j+1,1}^\dagger b_{j,2} - \text{H.c.}). \end{aligned} \quad (\text{A.4})$$

Thus, we can rewrite  $\mathbf{J}_x$  as

$$\mathbf{J}_x = \sum_j \left( j_{j,1}^\parallel + j_{j,2}^\parallel + \frac{1}{2} j_{2j-1}^\perp - \frac{1}{2} j_{2j}^\perp \right). \quad (\text{A.5})$$

We can observe that due to the triangular geometry of the ladder the current flowing in the  $x$ -direction has contributions also from the currents on the rungs. We note that a positive sign  $\mathbf{J}_x$  corresponds to a current flowing towards larger values of the site index  $j$ .

### Details on the numerical Matrix Product States methods

The numerical results presented in this work are obtained using a time-dependent matrix product state (tMPS) algorithm, which relies on the Trotter-Suzuki decomposition of the time evolution operator [68–70]. The

initial state of the evolution corresponds to the ground state of the model, [Eq. (1) in the main text], and has been determined using the density matrix renormalization group (DMRG) algorithm in the matrix product state (MPS) representation [70, 71]. Our implementations of the algorithms make use of the ITensor Library [72]. We consider the dynamics of hardcore bosons, with a local dimension of two states, for ladders with a number of rungs of  $L = 90$ . For the time-dependent results we take a maximal bond dimension up to 400 states, which ensures that the truncation error is at most  $10^{-9}$  at the final time of the evolution. We employ a time step of  $dtJ = 0.01$  and measure the observables every tenth time step. We note that for the ground state calculations presented in the following sections we considered larger system sizes and corresponding bond dimensions, the values can be found in the captions of the figures.

### Ground state phase diagram for hardcore bosons

In this section, we present the results for the ground state of the model of hardcore bosons on the triangular flux ladder given in Eq. (1) of the main text. The analysis of the numerical results used to determine the phase diagram follows Ref. [59], in which we consider similar parameters. In order to determine the nature of the chiral phases we consider the following observables. From the local currents, Eq. (A.4), we compute the chiral current  $J_c$  and the average rung current  $J_r$

$$J_c = \frac{1}{2(L-1)} \sum_j \langle j_{j,1}^\parallel - j_{j,2}^\parallel \rangle, \quad (\text{C.1})$$

$$J_r = \frac{1}{2L-1} \sum_j \langle |j_j^\perp| \rangle.$$

The biased phase is characterized by a finite density imbalance

$$\Delta n = \frac{1}{2L} \sum_j (n_{j,1} - n_{j,2}). \quad (\text{C.2})$$

Furthermore, we calculate the central charge  $c$ , which we extract from the scaling of the von Neumann entanglement entropy  $S_{vN}(l)$  of subsystem of length  $l$  embedded in the chain of length  $L$ . For open boundary conditions the entanglement entropy for the ground state of gapless phases is given by [73–75]

$$S_{vN} = \frac{c}{6} \log \left( \frac{L}{\pi} \sin \frac{\pi l}{L} \right) + s_1, \quad (\text{C.3})$$

where  $s_1$  is a non-universal constant and we have neglected corrections due to the finite size of the system [76, 77].

For the parameters considered in this work we find a rich diagram [59] of chiral phases, whose current patterns



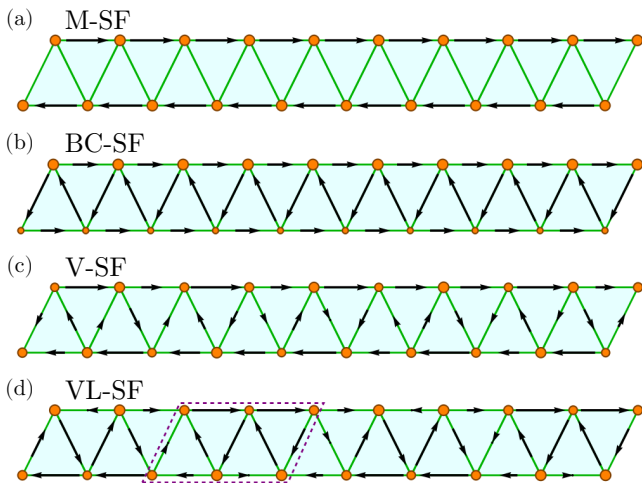


FIG. C1: The local current pattern, depicted with arrows, and on-site densities, depicted with orange disks, obtained in the ground state for the (a) Meissner superfluid (M-SF), (b) biased chiral superfluid (BC-SF), (c) vortex superfluid phases (V-SF), and (d) vortex lattice superfluid with  $\rho_v = 0.8$  (VL-SF). We note that we did not normalize the local currents to the same value for the different phases presented. In panel (d) we mark the periodic structure in the rung currents pattern.

are depicted in Fig. C1. We focus on the following phases in our study of the Hall response:

- The *Meissner superfluid* (M-SF), characterized by strong chiral currents on the legs and vanishing currents on the rungs, see Fig. C1(a). This state has one gapless mode and a central charge  $c = 1$ .
- The *biased chiral superfluid* (BC-SF), this phase breaks the  $\mathbb{Z}_2$  symmetry of the ladder and is characterized by a density imbalance. The currents on the legs flow in the same direction, however their different magnitude determine a finite chiral current, while on the rungs we have a strong current in the opposite direction, Fig. C1(b). The central charge is  $c = 1$ .
- The *vortex superfluid* (V-SF) has finite currents both on the legs and the rungs of the ladder. The currents determine a vortex density incommensurate with the ladder [Fig. C1(c)], which scales linearly with the flux  $\rho_v = \chi/\pi$ . In the VSF both modes are gapless and  $c = 2$ .
- If the vortices are pinned by the ladder and the vortex density becomes commensurate with the ladder we have a *vortex lattice superfluid* (VL-SF), e.g. Fig. C1(d) for  $\rho_v = 0.8$ . The central charge is  $c = 1$ .

We note that we extract the vortex density from the frequency corresponding to the peaks of the Fourier trans-

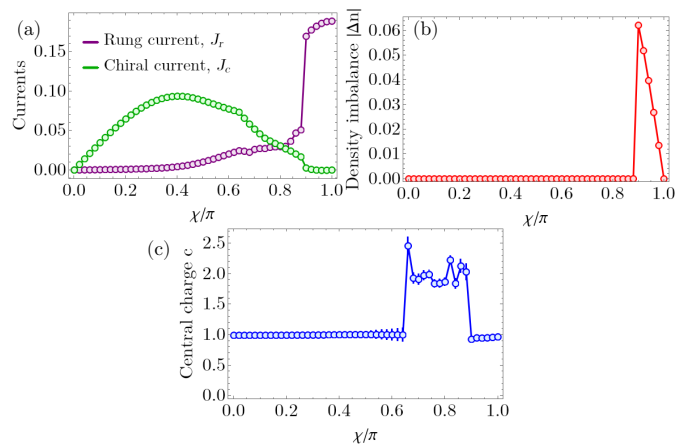


FIG. C2: Ground state results for (a) the average rung current,  $J_r$ , and the chiral current,  $J_c$ , (b) the absolute value of the density imbalance,  $|\Delta n|$ , and (c) the central charge,  $c$ , as a function of the flux  $\chi$  for  $J_{\parallel}/J = 0.6$ ,  $\rho = 0.25$ ,  $L = 120$ . We observe a transition from the Meissner superfluid to the vortex superfluid at  $\chi \approx 0.65\pi$ , and to the biased chiral superfluid at  $\chi \approx 0.88\pi$ . The maximal bond dimension used was  $m = 750$ .

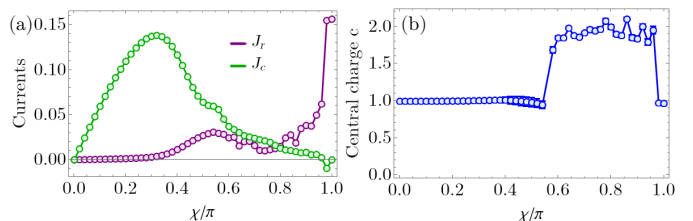


FIG. C3: Ground state results for (a) the average rung current,  $J_r$ , and the chiral current,  $J_c$ , and (b) the central charge,  $c$ , as a function of the flux  $\chi$  for  $J_{\parallel}/J = 1$ ,  $\rho = 0.25$ ,  $L = 120$ . We observe a transition from the Meissner superfluid to the vortex superfluid at  $\chi \approx 0.56\pi$ , and to the biased chiral superfluid at  $\chi \approx 0.97\pi$ . The maximal bond dimension used was  $m = 750$ .

form of the space dependence of the rung currents,  $j_l^\perp$  [59].

For a filling of  $\rho = 0.25$ , corresponding to the results presented in Fig. 1(b) and Fig. 2 in the main text, at small values of the flux  $\chi$ , or at small values of  $J_{\parallel}/J$ , we identify the Meissner superfluid phase. This can be concluded from the finite values of  $J_c$  and vanishing  $J_r$  as observed in Fig. C2(a) for  $J_{\parallel}/J = 0.6$  and Fig. C3(a) for  $J_{\parallel}/J = 1$ , together with a value consistent with  $c = 1$  for the central charge [Fig. C2(c) and Fig. C3(b)]. By increasing the flux, or  $J_{\parallel}/J$  [see the phase diagram shown in Fig. 1(b) of the main text] we enter the vortex superfluid, with finite values for both  $J_r$  and  $J_c$  [Fig. C2(a) for  $J_{\parallel}/J = 0.6$ , Fig. C3(a) for  $J_{\parallel}/J = 1$ ] and  $c \approx 2$  [Fig. C2(c) and Fig. C3(b)]. In the strongly frustrated regime, for  $\chi$  close to  $\pi$ , we can find the biased chiral superfluid. This phase has the largest extend for  $J_{\parallel}/J = 0.6$  and can be identified due to its finite den-

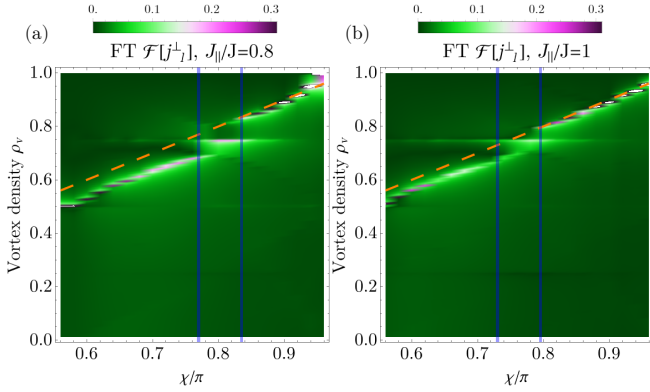


FIG. C4: The Fourier transform of the ground state local rung currents,  $j_j^\perp$ , as a function of the flux  $\chi$  for (a)  $J_\parallel/J = 0.8$ , (b)  $J_\parallel/J = 1$ ,  $\rho = 0.25$ ,  $L = 120$ . The vertical axis has been scaled in terms of the vortex density  $\rho_v$ . The results correspond to the vortex superfluid phase, where we expect  $\rho_v = \chi/\pi$  (depicted with orange dashed lines). The vertical blue lines mark the region in which the vortex density component  $\rho_v = 0.75$  dominates the Fourier transform.

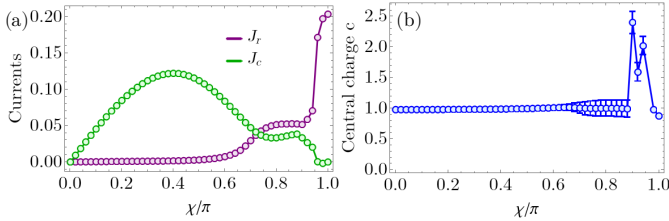


FIG. C5: Ground state results for (a) the average rung current,  $J_r$ , and the chiral current,  $J_c$ , and (b) the central charge,  $c$ , as a function of the flux  $\chi$  for  $J_\parallel/J = 0.6$ ,  $\rho = 0.4$ ,  $L = 120$ . We observe a transition from the Meissner superfluid to the vortex lattice superfluid with  $\rho_v = 0.8$  at  $\chi \approx 0.67$ , followed by a transition to the vortex superfluid at  $\chi \approx 0.89$ , and to the biased chiral superfluid at  $\chi \approx 0.97$ . The maximal bond dimension used was  $m = 750$ .

sity imbalance between the two legs of the ladder, see Fig. C2(b).

One interesting feature of the vortex superfluid phase for hardcore bosons on the triangular ladder, which we identified in Ref. [59], is the presence of a second peak in the Fourier transform of the local rung currents, besides the one corresponding to a vortex density  $\rho_v \approx \chi/\pi$ . We connected the value of vortex density corresponding to the second peak to the atomic filling,  $\rho_v = (1 - \rho)$ , as we can observe in Fig. C4. Surprisingly, there exists a region in which the vortex density related to the atomic filling has the stronger contribution to the Fourier transform of the rung currents [marked by vertical blue lines in Fig. C4(a) for  $J_\parallel/J = 0.8$  and Fig. C4(a) for  $J_\parallel/J = 1$ ]. However, this does not induce a pinning of the vortices and a gapped mode, as the central charge is  $c \approx 2$ , this can be seen in Fig. C3(b) for  $0.73\pi \lesssim \chi \lesssim 0.79\pi$ . Thus, the nature remains that of an incommensurate vortex

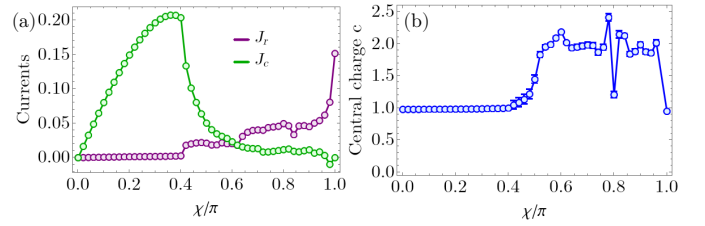


FIG. C6: Ground state results for (a) the average rung current,  $J_r$ , and the chiral current,  $J_c$ , and (b) the central charge,  $c$ , as a function of the flux  $\chi$  for  $J_\parallel/J = 1$ ,  $\rho = 0.4$ ,  $L = 120$ . We observe a transition from the Meissner superfluid to the vortex lattice superfluid with  $\rho_v = 0.6$  at  $\chi \approx 0.41\pi$ , followed by a transition to the vortex superfluid at  $\chi \approx 0.5\pi$ , between  $\chi \approx 0.79$  and  $\chi \approx 0.81\pi$  we have a vortex lattice superfluid with  $\rho_v = 0.8$ , and from  $\chi \approx 0.97\pi$  the biased chiral superfluid. The maximal bond dimension used was  $m = 750$ .

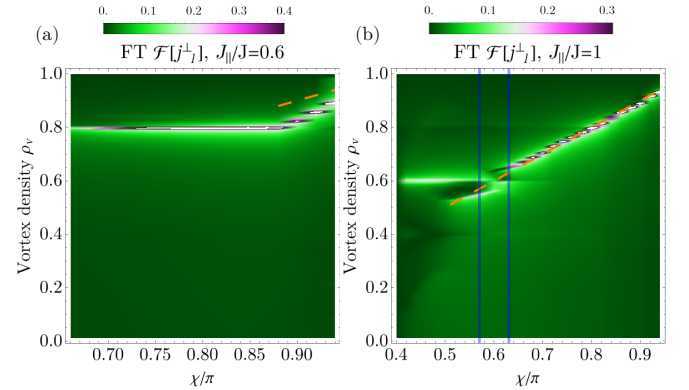


FIG. C7: The Fourier transform of the ground state local rung currents,  $j_j^\perp$ , as a function of the flux  $\chi$  for (a)  $J_\parallel/J = 0.6$ , (b)  $J_\parallel/J = 1$ ,  $\rho = 0.4$ ,  $L = 120$ . The vertical axis has been scaled in terms of the vortex density  $\rho_v$ . The orange dashed lines corresponds to the expectation of the vortex superfluid phase of  $\rho_v = \chi/\pi$ . In (b) the vertical blue lines mark the region in which the vortex density component  $\rho_v = 0.6$  dominates the Fourier transform in the VSF.

phase. The presence of the second vortex density will be further discussed in the following section.

In the case of atomic filling of  $\rho = 0.4$ , beside the three phases previously discussed, we can also find vortex phases with a commensurate vortex density, i.e. vortex lattice superfluid, which we did not observe for the parameters of Ref. [59]. For  $\rho = 0.4$  and  $J_\parallel/J = 0.6$  as we increase the flux from the Meissner phase around  $\chi \approx 0.67\pi$  we enter a phase with finite rung and chiral currents and  $c = 1$ , as shown in Fig. C5. If we compute the vortex density, Fig. C7(a), we obtain for  $0.67\pi \lesssim \chi \lesssim 0.89\pi$  a commensurate value of  $\rho_v = 0.8$ . This implies the existence of a vortex lattice superfluid phase with  $\rho_v = 4/5$ , the commensurate vortex pattern is shown in Fig. C1(d). Similarly, for  $J_\parallel/J = 1$ , Fig. C6, we find at  $\chi \approx 0.41\pi$  a transition from the Meissner phase to a vortex lattice superfluid phase with  $\rho_v = 0.6$ . In-

terestingly, if we look at the Fourier transform of the rung currents in Fig. C7(b), we observe that between  $0.41\pi \lesssim \chi \lesssim 0.5\pi$  we have only  $\rho_v = 0.6$ , while after entering the vortex superfluid we have both  $\rho_v = 0.6$  and  $\rho_v \approx \chi/\pi$ . And while for  $0.57\pi \lesssim \chi \lesssim 0.63\pi$   $\rho_v = 0.6$  has a larger weight in the Fourier transform, the state remains gapless with  $c \approx 2$  [see Fig. C6(b)]. At larger values of the flux  $\chi \gtrsim 0.7\pi$  we only observe the incommensurate vortex density. However, in the central charge around  $\chi \approx 0.8\pi$  we see a deep towards  $c = 1$  [Fig. C6(b)] indicating the possibility of a narrow vortex lattice with  $\rho_v = 0.8$ , connected to the one present at lower values of  $J_{\parallel}/J$ .

### Origin of commensurate vortex density: going between free fermions and hardcore bosons

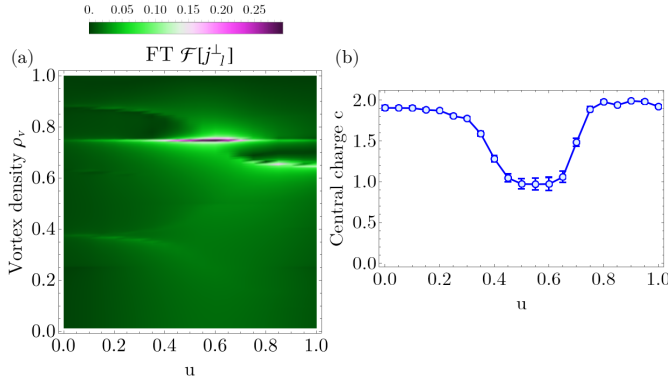


FIG. D1: (a) The Fourier transform of the ground state local rung currents,  $j_j^\dagger$ , and (b) the central charge,  $c$ , as a function of the interaction  $u$ , for  $J_{\parallel}/J = 1$ ,  $\chi = 0.7\pi$ ,  $\rho = 0.25$ ,  $L = 120$ . In (a) the vertical axis has been scaled in terms of the vortex density  $\rho_v$ .

One approach to deal with a model of hardcore bosons is to employ the Jordan-Wigner transformation to spinless fermions

$$b_j = \prod_{l=1}^{j-1} e^{i\pi c_l^\dagger c_l} c_j, \quad (\text{D.1})$$

where  $c_j$  are fermionic operators. In order to use this transformation we first rewrite the Hamiltonian, Eq. (1) in the main text, on a chain along the rungs of the triangular ladder

$$H_{\text{chain}} = -J \sum_j \left( b_j^\dagger b_{j+1} + \text{H.c.} \right) - J_{\parallel} \sum_j \left[ e^{i(-1)^j \chi} b_j^\dagger b_{j+2} + \text{H.c.} \right]. \quad (\text{D.2})$$

In the language of fermionic operators, using Eq. (D.1),

we obtain

$$H_f = -J \sum_j \left( c_j^\dagger c_{j+1} + \text{H.c.} \right) - J_{\parallel} \sum_j \left[ e^{i(-1)^j \chi} c_j^\dagger (1 - 2c_{j+1}^\dagger c_{j+1}) c_{j+2} + \text{H.c.} \right]. \quad (\text{D.3})$$

We observe that due to the hopping term over two sites, stemming from the triangular geometry, the Jordan-Wigner string does not cancel and gives rise to an interaction term. Thus, the hardcore bosons are not mapped to free fermions on the triangular ladder and we obtain an interacting fermionic model.

In order to gauge the importance of the four-fermion interaction term, in the following we vary its strength

$$H_f(u) = -J \sum_j \left( c_j^\dagger c_{j+1} + \text{H.c.} \right) - J_{\parallel} \sum_j \left[ e^{i(-1)^j \chi} c_j^\dagger (1 - 2uc_{j+1}^\dagger c_{j+1}) c_{j+2} + \text{H.c.} \right]. \quad (\text{D.4})$$

In the limit of  $u = 0$  the model reduces to free fermions on a triangular flux ladder, while for  $u = 1$  we recover the hardcore bosons.

In Fig. D1 we study the nature of the ground state as a function of  $u$ . At intermediate values of the interaction,  $0.4 \lesssim u \lesssim 0.7$ , we observe a strong peak in the Fourier transform of the local rung currents at a vortex density of  $\rho_v = 0.75$ . This fact together with the value of the central charge of  $c \approx 1$  in this regime points towards the existence of a vortex lattice phase in the interacting fermion model. Interestingly, the peak at  $\rho_v = 0.75$  does not vanish when we enter the gapless  $c = 2$  phases, either towards free fermions, or hardcore bosons. Thus, this suggests that the origin of the vortex density commensurate with the filling stems from the interplay of interactions and the triangular geometry, due to the proximity of the vortex lattice with  $\rho_v = 0.75$ .

We note that the local rung currents have an analogous definition for fermions and hardcore bosons, as they connect neighboring sites in the chain representation the Jordan-Wigner string vanishes. This makes them a relevant observable to analyze as we vary  $u$  to go from free fermions to hardcore bosons in our system.

### Time dependence of the Hall Polarization

In this section we present additional numerical data for the behavior of the Hall polarization,  $P_H$ , supporting the results we discussed in the main text. In the following, we show the time evolution of  $P_H$  in the different phases, from which we extracted the time-averaged  $\langle\langle P_H \rangle\rangle$  depicted in the figures of the main text. Furthermore, we plot the time dependence of the current  $\mathbf{J}_x$  and imbalance  $P_y$  used in the calculation of  $P_H$ . Finally, we

analyze the influence of the strength of the linear potential quenched in the protocol, which gives us a handle also on the finite size effects present in the simulations.

We note that in order to limit the influence of the finite size effects we compute the current  $\mathbf{J}_x$  and imbalance  $P_y$  for a subsystem of length  $L/3$  in the middle of our system. We found that this represents a good trade-off of having enough lattice sites to compute reliably the observables and access to the dynamics of to long enough times before we observe the finite size effects of the particles being reflected by the boundaries.

### Hall Polarization in the Meissner superfluid phase

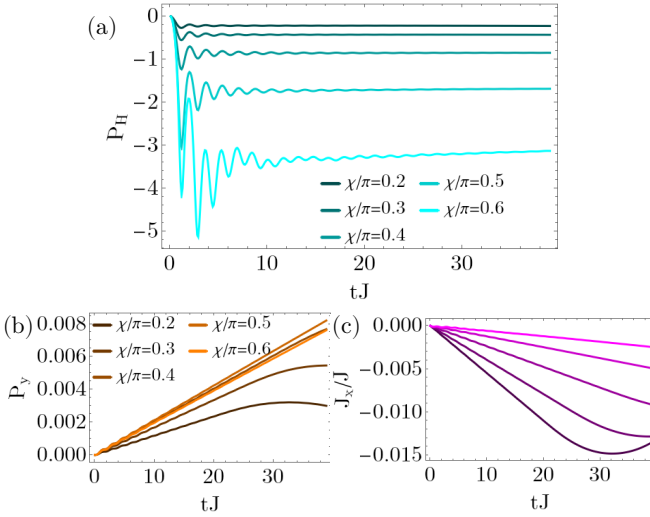


FIG. E1: (a) The time evolution of  $P_H$  in the Meissner superfluid phase for several values of the flux  $\chi \in \{0.2\pi, 0.3\pi, 0.4\pi, 0.5\pi, 0.6\pi\}$ . The time evolution of (b)  $P_y$  and (c)  $\mathbf{J}_x$  for the same values of the flux, where the lightest shade of (b) orange and (c) magenta corresponds to  $\chi = 0.6\pi$  and the colors are gradually darker for the smaller values of  $\chi$ . The parameters used are  $J_{\parallel}/J = 0.6$ ,  $L = 90$  rungs,  $\rho = 0.25$  and  $\mu/J = 0.001$ .

In Fig. E1(a) we plot the dynamics of the Hall polarization in the Meissner phase. We observe for all values of the flux a well-defined plateau occurring after the initial increase and damped oscillations. As we increase  $\chi$  towards the transition threshold to the vortex phase at  $\chi \approx 0.65\pi$ , both the value of the late-time plateau increases (as discussed in the main text) and the amplitude of the oscillations. The large values of  $P_H$  close to the phase transition stems from the decrease of the magnitude of the current  $\mathbf{J}_x$ . We can see in Fig. E1(c) that the smallest values of the current correspond to  $\chi = 0.6\pi$  (lightest shade of magenta), while the imbalance  $P_y$  has similar values for  $\chi = 0.4\pi$ ,  $\chi = 0.5\pi$  and  $\chi = 0.6\pi$  [Fig. E1(b)].

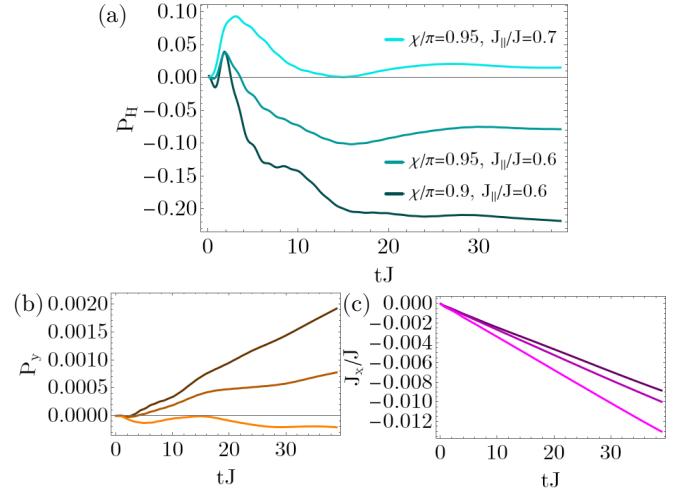


FIG. E2: (a) The time evolution of  $P_H$  in the biased chiral superfluid phase for several values of the flux  $\chi = 0.95\pi$ ,  $J_{\parallel}/J = 0.7$ , and  $\chi \in \{0.9\pi, 0.95\pi\}$ ,  $J_{\parallel}/J = 0.6$ . The time evolution of (b)  $P_y$  and (c)  $\mathbf{J}_x$  for the same values of the flux and  $J_{\parallel}$ , where the lightest shade of (b) orange and (c) magenta corresponds to the lightest shade of cyan in (a). The parameters used are  $L = 90$  rungs,  $\rho = 0.25$  and  $\mu/J = 0.001$ .

For  $\chi = 0.2\pi$  we see in both  $P_y$  and  $\mathbf{J}_x$  [Fig. E1(b)-(c)] that around  $tJ \approx 30$  a change in the monotony occurs, we attribute this to finite size effects. However,  $P_H$  shows a robust plateau up to these times, such that we can use this behavior to determine the longest times that we can use in the time averaged quantity  $\langle\langle P_H \rangle\rangle$ . We can also observe that for the larger values of the flux the extremum of the currents occurs at even longer times.

### Hall Polarization in the biased chiral superfluid phase

The time evolution of  $P_H$  in the biased chiral superfluid, shown in Fig. E2(a), exhibits a very different dynamics compared to the Meissner phase. The saturation process is much slower, only after  $tJ \approx 15$  we observe a constant-like value, but which still has low frequency and small amplitude oscillations on top [in contrast to the oscillations of the M-SF seen in Fig. E1(a)]. This behavior seems to stem from the dynamics of the density imbalance  $P_y$ , as seen in Fig. E2(b), which shows oscillations with a small frequency, while the current, Fig. E2(c), has a mostly linear dependence on time. Furthermore, in the BC-SF we obtain both negative and positive values of  $P_H$ , a sign change happening for  $\chi = 0.95\pi$  as we increase  $J_{\parallel}/J = 0.6$  to  $J_{\parallel}/J = 0.7$  [see Fig. E2(a)].

### Hall Polarization in the vortex superfluid phase

A change of the sign of the value at which  $P_H$  stabilizes occurs also in the vortex superfluid, see Fig. E3 and the

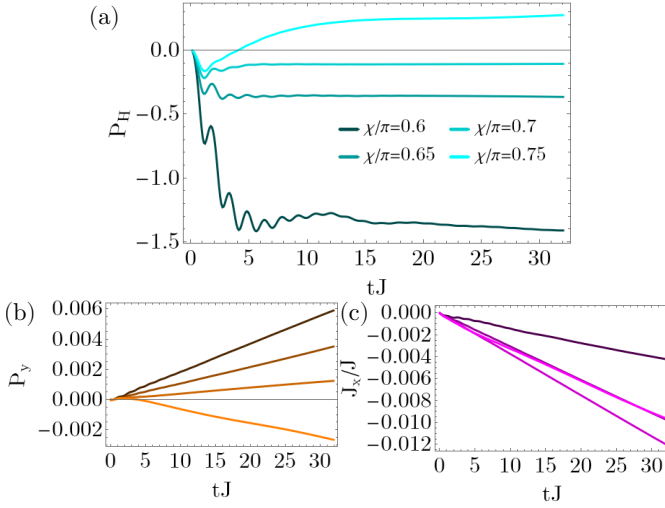


FIG. E3: (a) The time evolution of  $P_H$  in the vortex superfluid phase for several values of the flux  $\chi \in \{0.6\pi, 0.65\pi, 0.7\pi, 0.75\pi\}$ . The time evolution of (b)  $P_y$  and (c)  $J_x$  for the same values of the flux and  $J_{\parallel}$ , where the lightest shade of (b) orange and (c) magenta corresponds to the lightest shade of cyan in (a). The parameters used are  $J_{\parallel}/J = 0.8$ ,  $L = 90$  rungs,  $\rho = 0.25$  and  $\mu/J = 0.001$ .

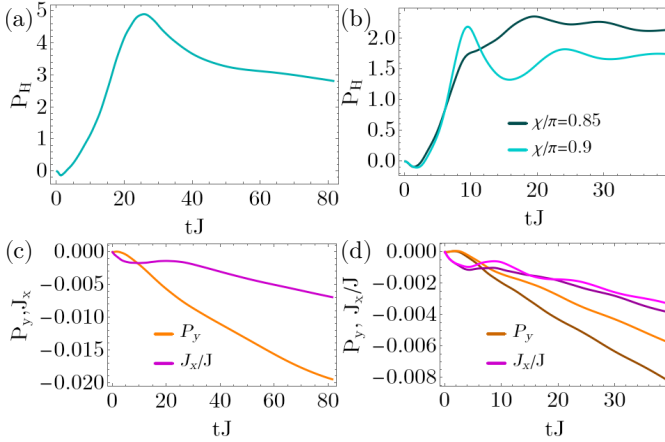


FIG. E4: (a)-(b) The time evolution of  $P_H$  in the vortex superfluid phase for (a)  $\chi = 0.8\pi$ , (b)  $\chi = 0.85\pi$  and  $\chi = 0.9$ . (c)-(d) The time evolution of  $P_y$  and  $J_x$  for (c)  $\chi = 0.8\pi$ , (d)  $\chi = 0.85\pi$  and  $\chi = 0.9$ . In panel (d) the lightest shade of orange and magenta corresponds to the lightest shade of cyan in (b). The parameters used are  $J_{\parallel}/J = 0.8$ ,  $L = 90$  rungs,  $\rho = 0.25$  and  $\mu/J = 0.001$ .

main text. After the transition from the Meissner phase, occurring at  $\chi \approx 0.59\pi$  for  $J_{\parallel}/J = 0.8$ , the magnitude of  $\langle\langle P_H \rangle\rangle$  decreases and reaches values close to zero around  $\chi \gtrsim 0.7\pi$  [Fig. E3(a)]. If we continue to increase the flux,  $P_y$  changes sign which determines positive values for  $P_H$  [Fig. E3(b)]. We can observe for  $\chi = 0.75\pi$  in Fig. E3(a) that initially  $P_H$  is negative and only at longer times it becomes positive and that the steady plateau is reached on a longer time scale than for the smaller values of the

flux. The time scales for reaching a plateau are even longer for larger values of the flux, as seen in Fig. E4(a) for  $\chi = 0.8\pi$  and Fig. E4(b) for  $\chi = 0.85\pi, 0.9\pi$ . In particular, for  $\chi = 0.8\pi$  we obtain one of the largest positive values for  $P_H$  throughout the phase diagram, due to the commensurate effects present in the vortex superfluid discussed in the previous sections. For this value of the flux, in Fig. E4(a) we observe that  $P_H$  increases up to  $tJ \approx 25$  and only afterwards decreases towards a saturation value. However, as the saturation only occurs at very long times, the finite size effects play a noticeable role.

#### Hall Polarization in the vortex lattice superfluid phase

For an atomic density of  $\rho = 0.4$  we identified vortex lattice superfluid phase with vortex densities  $\rho_v = 0.8$  and  $\rho_v = 0.6$  and  $\langle\langle P_H \rangle\rangle$  in these phases was shown in Fig. 3(b) of the main text. In Fig. E5 we show the time dependence of the Hall polarization in these phases. We observe in Fig. E5(a) for  $J_{\parallel}/J = 0.6$  after we cross the phase boundary at  $\chi \approx 0.67\pi$  from the Meissner superfluid into the vortex lattice superfluid with  $\rho_v = 0.8$   $P_H(t)$  saturates to large negative values and exhibits a prominent peak at short times,  $tJ \approx 2$  followed by damped oscillations. For  $J_{\parallel}/J = 1$  and  $\chi = 0.5\pi$  in Fig. E5(b) we are in the vortex lattice superfluid phase with  $\rho_v = 0.6$ . We can see that the dynamics in the vortex lattice superfluid phases does not resemble the one in the vortex superfluid in the region where we have the additional commensurate vortex density related to the density, which can be seen for  $\chi = 0.6\pi$  in Fig. E5(b).

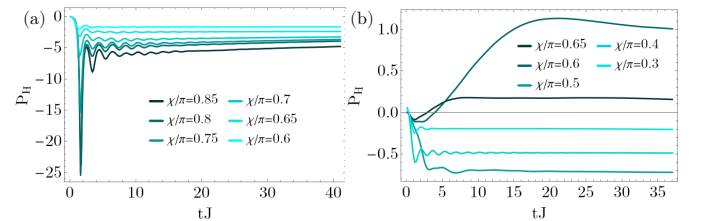


FIG. E5: (a)-(b) The time evolution of  $P_H$  for  $\rho = 0.4$  and several values of  $\chi$  with (a)  $J_{\parallel}/J = 0.6$ , and (b)  $J_{\parallel}/J = 1$ . For  $J_{\parallel}/J = 0.6$ , a phase transition between the Meissner superfluid and the vortex lattice superfluid with  $\rho_v = 0.8$  at  $\chi \approx 0.67\pi$ . For  $J_{\parallel}/J = 1$  a succession of phase transitions from the Meissner superfluid, to the vortex lattice superfluid with  $\rho_v = 0.6$  and to the vortex superfluid occur at  $\chi \approx 0.41\pi$  and  $\chi \approx 0.51\pi$ . The parameters used are  $L = 90$  rungs and  $\mu/J = 0.001$ .

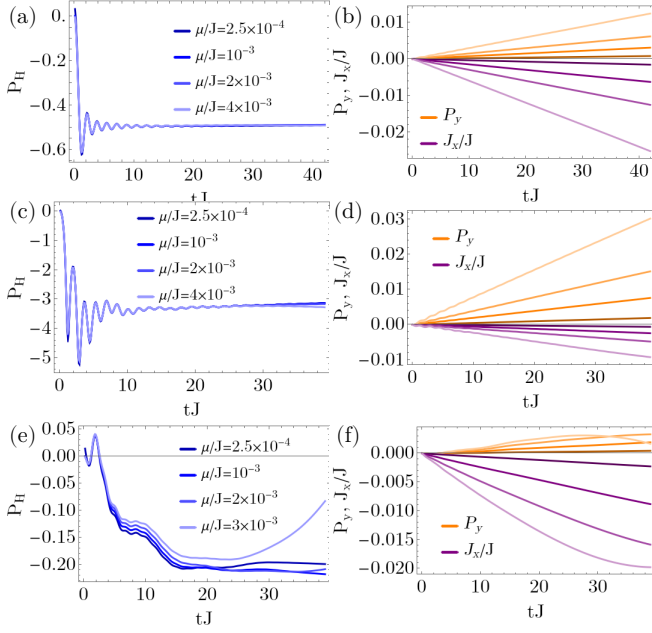


FIG. E6: The time evolution of  $P_H$ ,  $P_y$  and  $J_x$  for several values of the strength of the linear potential  $\mu/J$ , for (a)-(b)  $J_{\parallel}/J = 0.2$  and  $\chi = 0.65\pi$ , (c)-(d)  $J_{\parallel}/J = 0.6$  and  $\chi = 0.6\pi$  in the Meissner superfluid, and (e)-(f)  $J_{\parallel}/J = 0.6$  and  $\chi = 0.9\pi$  in the biased chiral superfluid. In the panels on the right depicting  $P_y$  and  $J_x$ , going from the lightest to the darkest shades of orange and purple corresponds to the legends in the panels on the left depicting  $P_H$ . The parameters used are  $L = 90$  rungs and  $\rho = 0.25$ .

#### Influence of the linear potential and finite size effects

In this section we analyze the consistency of our results for the dynamics of the Hall polarization under the variation of the strength of the linear potential  $\mu$  quenched in the protocol described in the main text. Furthermore, as the strength of the potential determines the magnitude of the current flowing through the ladder, it can be used also to infer the finite size effects in our results. For stronger potentials, which induce a current  $J_x$  growing faster in time, the boundary effects will be noticeable at shorter times, compared to the weaker potentials. Thus, we used a value of  $\mu/J = 10^{-3}$  in the main text which allowed us to capture the long time dynamics of  $P_H$ .

In the Meissner phase, Fig. E6(a),(c), we see very little dependence while varying the potential with more than an order of magnitude, from  $\mu/J = 2.5 \times 10^{-4}$  to  $\mu/J = 4 \times 10^{-3}$ . The results in the biased chiral superfluid are more sensitive to the strength of the potential, for  $\mu/J = 3 \times 10^{-3}$  we observe in Fig. E6(e) that  $P_H$  starts increasing from  $tJ \approx 25$ , behavior which is not present for smaller values of the potential and we can attribute to the finite size of the system. However, for  $\mu/J = 2.5 \times 10^{-4}$  to  $\mu/J = 2 \times 10^{-3}$  the behavior of  $P_H$  is consistent for the different values and only small shifts

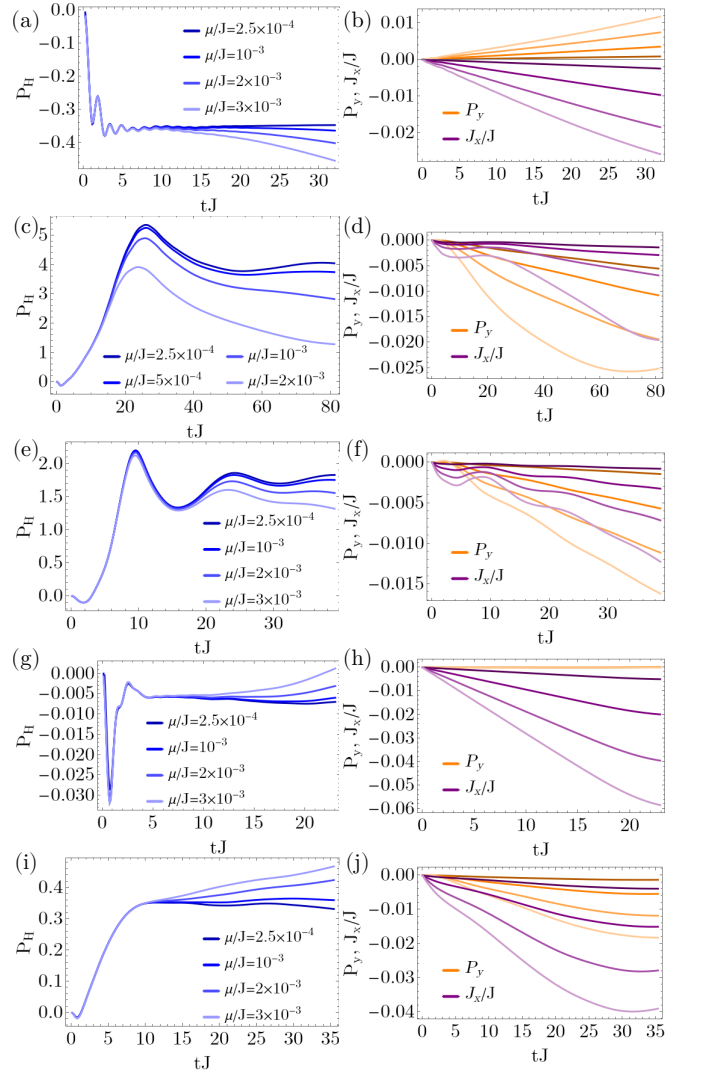


FIG. E7: The time evolution of  $P_H$ ,  $P_y$  and  $J_x$  for several values of the strength of the linear potential  $\mu/J$  in the vortex superfluid phase, for (a)-(b)  $J_{\parallel}/J = 0.8$  and  $\chi = 0.65\pi$ , (c)-(d)  $J_{\parallel}/J = 0.8$  and  $\chi = 0.8\pi$ , (e)-(f)  $J_{\parallel}/J = 0.8$  and  $\chi = 0.9\pi$ , (g)-(h)  $J_{\parallel}/J = 1.3$  and  $\chi = 0.65\pi$ , and (i)-(j)  $J_{\parallel}/J = 1.3$  and  $\chi = 0.8\pi$ . In the panels on the right depicting  $P_y$  and  $J_x$ , going from the lightest to the darkest shades of orange and purple corresponds to the legends in the panels on the left depicting  $P_H$ . The parameters used are  $L = 90$  rungs and  $\rho = 0.25$ .

are present for  $tJ \gtrsim 8$ .

In Fig. E7 in the vortex superfluid phase, we can see that for smaller values of  $\mu$  we obtain a steady plateau in  $P_H(t)$  for longer times and the point in time where we see deviations from this value is determined by the value of  $\mu$ . This holds for different parameters in the vortex phase, as we show in Fig. E7, which exemplifies the different behaviors we obtained. In particular, we observe in Fig. E7(c) and Fig. E7(e), corresponding to the regime of large positive values of the Hall response,

that for lower values of  $\mu$  the value of  $P_H$  is higher. In Fig. E7(c) where we need to go to very long times,  $P_H$  for the value we used in the main text of  $\mu/J = 10^{-3}$  shows deviations which underestimate the saturation value of the Hall polarization, compared to the results for  $\mu/J =$

$2.5 \times 10^{-4}$  and  $\mu/J = 5 \times 10^{-4}$ . Thus, the features of large positive values of the Hall response discussed in the main text are even more pronounced if one extrapolates the results in the limit of small potential strengths and larger system sizes.